Design of a Lamb-shift polarimeter for pulsed intense polarized H^+/D^+ ion sources*

Yaojie Zhai,[1,2] Sheng Zhang,[1,2] Boxing Gou,[1,2] Xuezhen Zhang,[1] Yuguo Liu,[1] Qianyu Jin,[1,2,†] and Liangting Sun[1,2,‡]

[1] *Institute of Modern Physics, Chinese Academy of Sciences, Lanzhou 730000, China*

[2] *School of Nuclear Science and Technology, University of Chinese Academy of Sciences, Beijing 100049, China*

An intense spin polarized H^+/D^+ ion source (SPIS) based on the principle of atomic beam source and resonant plasma ionizer is under development at Institute of Modern Physics (IMP, CAS) for the future Electron-ion collider in China (EicC). In order to measure the polarization of the pulsed H^+/D^+ beam extracted from the SPIS at an energy of $25\,\mathrm{keV}$, a Lamb-shift polarimeter (LSP) has been designed. Compared with the polarization measurement utilizing nuclear reactions that demands polarized ion beam accelerated to the MeV level, LSP operated at a low energy is evidently more convenient. Moreover, thanks to its principle, LSP can function normally even in the presence of a mixed H_2^+ component in the extracted polarized D^+ beam, which is inevitable for the polarized ion source utilizing resonant plasma ionizer. An ion beam transport system aiming at modifying the beam spin orientation and decelerating the beam from $25\,\mathrm{keV}$ to $2.5\,\mathrm{keV}$ is incorporated into the LSP, which enables the LSP to be used directly at downstream of the SPIS. In this work, all of the involved critical physical processes and components of the LSP have been modeled, analyzed and designed carefully to ensure high efficiency at each stage of its operation. Even for a low duty factor pulsed ion beam, the LSP is capable of measuring the polarization with a precision of $1\,\%$ in a few seconds.

Keywords: Spin polarization, Polarized ion source, Lamb-shift polarimeter

I. INTRODUCTION

The electron-ion collider has been recognized as an ideal tool to explore the inner structure and interactions of the nucleons and nuclei. The Electron-ion collider in China (EicC) has been proposed and is under conceptual design phase [1, 2]. The EicC is suggested to be built by upgrading the High Intensity heavy-ion Accelerator Facility (HIAF) which is currently under construction [3, 4]. The featured physics at EicC includes the emergence of the proton spin and mass, the nucleon partonic structure, exotic hadron states, *etc*. To pursue such scientific goals, EicC is conceptually designed to deliver high luminosity collisions involving highly polarized electron, proton and light ions [5–7]. Therefore, it is essential for the EicC to achieve production, acceleration and preservation of polarized ion and electron beams. Some research and development (R&D) projects such as key technologies prototyping have already been initiated to support these objectives. [8]. As one of the R&D projects for EicC, a spin polarized ion source (SPIS) to produce intense H^+/D^+ beams with high polarization is under development at Institute of Modern Physics (IMP, CAS).

Technologies of polarized ion source have undergone significant development since the 1960s, culminating in considerable progress to the present day. Modern polarized ion sources generate polarized ion beams with intensity of mA level and polarization of about $80\,\%$. In polarized ion sources, the process always involves the generation of atoms with polarized nuclei followed by ionization to produce polarized ions. At present, atomic beam-type and optically pumped polarized ion sources (ABPIS and OPPIS), classified by polarized atom generation, are mainly used to provide polarized ion beam to accelerator. There are different ionization schemes available for ABPIS and OPPIS to produce positive or negative polarized ions. Performances of several typical polarized ion sources are listed in table. 1. Status of polarized ion sources development has been reviewed in refs. [9, 10].

The SPIS developed at IMP is based on the principle of atomic beam source and resonant plasma ionizer. It is designed to produce polarized H^+/D^+ ion beam of $1\,\mathrm{mA}$, $25\,\mathrm{keV}$, with pulse width of $100\,\mu\mathrm{s}$, repetition frequency of $5\,\mathrm{Hz}$ and polarization of no less than $80\,\%$. The layout of the SPIS is shown in Fig. 1. The hydrogen molecules are injected into a dissociator (1) through a pulsed solenoid valve (15) and are dissociated into atoms with a radio-frequency (RF) discharge. The flow out channel of the dissociator is wrapped by a cold copper clip (2) which is cooled to 70 K by a refrigerator (3), so that the velocity dispersion of the atoms is reduced. The atomic beam is collimated by a skimmer (4). Two permanent sextupole magnets (5 and 7) and three RF transition units (6, 8, and 9) are used to polarize the atomic beam. By switching on specific sets of RF transition units, beams of desired polarization modes can be produced. The polarized H atoms and D^+ ions from deuterium plasma jet produced by an arc plasma source (14) are injected toward each other and intersect in a storage cell (13) where polarized protons are formed through the quasi-resonant charge exchange reactions [16],

$$\overrightarrow{H} + D^+ \rightarrow \overrightarrow{H^+} + D. \tag{1}$$

To avoid depolarization during the charge exchange, the storage cell is placed in a solenoid magnet (12), which generates a magnetic field of about $0.3\,\mathrm{T}$, much stronger than the critical field of the ground state hydrogen (deuterium) atom ($B^{1S}_{c,H} = 50.7\,\mathrm{mT}$, $B^{1S}_{c,D} = 11.7\,\mathrm{mT}$) [17]. Both, the polar-

* Supported by the National Key Research and Development Program of China (No. 2020YFE0202004, 2023YFA1606801), the National Natural Science Foundation of China (No.12375162) and the Natural Science Foundation of Gansu Province, China (No. 24JRRA039).

† Corresponding author, Qianyu Jin, Nanchang Road 509, Lanzhou, Gansu Province, PRC, jinqianyu@impcas.ac.cn.

‡ Corresponding author, Liangting Sun, Nanchang Road 509, Lanzhou, Gansu Province, PRC, sunlt@impcas.ac.cn.

Table 1. Performances of several typical polarized ion sources.

Year	Institute	Particle	Intensity	Duty Factor	Polarization	Polarization Acquisition	Ionizer
2007	INR, RAS [11]	H^+, H^-	$11\,\mathrm{mA}$, $4\,\mathrm{mA}$	$200\,\mu$s, $10\,\mathrm{Hz}$	90%	ABPIS	Plasma Ionizer
2014	BNL [10]	H^-	$4\,\mathrm{mA}$	$300\,\mu$s, $1\,\mathrm{Hz}$	85%	OPPIS	Na Jet
2007	FZJ [12]	H^-	$50\,\mu A$	$20\,\mathrm{ms}$, $0.5\,\mathrm{Hz}$	90%	ABPIS	Cs Beam
2018	JINR [13]	D^+	$6\,\mathrm{mA}$	$150\,\mu$s, $1\,\mathrm{Hz}$	88%	ABPIS	Plasma Ionizer
2002	IUCF [14]	H^-, D^-	$1.8\,\mathrm{mA}$, $2\,\mathrm{mA}$	$300\,\mu$s, $3\,\mathrm{Hz}$	90%	ABPIS	Plasma Ionizer
2023	BNL [15]	$^3He^{++}$	Goal: $2\,\mathrm{mA}$	$20\,\mu$s	70%	OPPIS	EBIS*

*Electron Beam Ion Source.

ized protons and the unpolarized deuterons are pulled out by a beam extraction system (11), and are spatially separated by a bending magnet (10). Their currents are measured by a Faraday cup (17) or a beam dump (16), respectively. Then the beam polarization is measured by a Lamb-shift polarimeter (18) assembled downstream the SPIS. When the SPIS is operated for a polarized deuteron beam, the inlet gas of the atomic beam source and of the plasma ionizer are switched. However, it is inevitable that the extracted polarized D^+ beam will be mixed with an unpolarized H_2^+ component since the D^+ and H_2^+ ions can't be separated by the bending magnet. Not until the beam is pre-accelerated can the H_2^+ ions be stripped into protons and then be swept out [13].

Beam polarization is one of the main quantities characterizing a polarized ion beam. For proton (spin-1/2) beams produced by an axially symmetric polarized ion source, it is sufficient to describe the polarization with the vector polarization,

$$P_z = n_+ - n_-, \tag{2}$$

where $n_\pm$ are the occupation numbers of protons with spin parallel and antiparallel to the quantization axis along z. For deuteron (spin-1) beams the tensor polarization,

$$P_{zz} = 1 - 3n_0, \tag{3}$$

is required in addition to fully describe their polarization states. Here n_0 is the occupation number of deuterons with spin perpendicular to z.

It is necessary to measure the beam polarization quickly and accurately downstream the SPIS for precise investigation of the spin depolarization in the subsequent acceleration, even for the operation of the SPIS. Utilizing suitable nuclear reactions with known and adequate analyzing power and cross section, beam polarization can be determined by the angular asymmetry of the reaction products. However, at the beam energy of $25\,\mathrm{keV}$, there are hardly any competent nuclear reactions. Unless, the beam is pre-accelerated before the polarization measurement [13, 18]. In this way, expensive accelerator time has to be used for optimizing and tuning the SPIS. Lamb-shift polarimeter (LSP) based on the atomic processes sensitive to the nuclear spin polarization is more preferred in the vicinity of several keV [19, 20]. Moreover, LSP can function normally despite the mixed H_2^+ component within the extracted polarized D^+ beam from the plasma ionizer. Therefore, a LSP is under intense development at IMP for measuring the polarization of the beam produced by the SPIS.

II. PRINCIPLES OF LAMB-SHIFT POLARIMETER

Spin filter is the core component of LSP. It was originally invented for the Lamb-shift polarized ion source (LSPIS) at Los Alamos National Laboratory (LANL) in the late 1960's [21]. Spin filter consists of a solenoid magnet providing an uniform magnetic field B_s parallel to the beam, and a cylindrical RF resonant cavity providing a longitudinal RF electric field E_{rf}, a transversal RF magnetic B_{rf} and a transversal static electric field E_s. Installed inside and coaxially with respect to the solenoid, the RF resonant cavity works in the mode of TM_{010} with a frequency of $1610\,\mathrm{MHz}$. It is divided into two pairs of opposing quadruplets. One pair is used for radio frequency (RF) power coupling and signal pick-up, and to the other a DC voltage is applied symmetrically. Spin filter utilizes a three-level resonance interaction among the $n = 2$ hyperfine states of the hydrogen (deuterium) atom, which was first reported in 1951 by Lamb and Retherford [22]. Hydrogen (deuterium) atoms in the 2S state are metastable with a lifetime of $1/7$ s. Atoms in the 2P state undergo an allowed electric-dipole decay with a lifetime of $1.6\,\mathrm{ns}$. Fig. 2 shows the $2S_{1/2}$ and $2P_{1/2}$ levels of the hydrogen atom in an external magnetic field with nuclear hyperfine structure included. The levels are labeled with α, β, e and f, based on the nomenclature first introduced by Lamb and Retherford [23]. The notation $|m_j, m_I\rangle$ indicates the spin projections of electron and proton in a strong magnetic field. The energies of states α and e (with electron spin parallel to the magnetic field, $m_j = 1/2$) increase with the magnetic field, while that of β and f ($m_j = -1/2$) decrease. In the region around $57.5\,\mathrm{mT}$, the β and e levels cross each other and the splitting between states α and β (e) is about $1610\,\mathrm{MHz}$. The transversal electric field E_s mixes states β and e, while the longitudinal RF electric field E_{rf} mixes α and e, which lead the lifetime of the metastable α and β to decrease sharply. In general, all metastable atoms in this region will be quenched into the ground state before they exit the spin filter. Exceptions occur when the α-β resonance is induced by the transversal RF magnetic field B_{rf}, which reduces the α-e resonance, allowing about $50\,\%$ of the atoms in α state to survive. Note that the width of the α-e resonance is approximately $7\,\mathrm{mT}$ depending on the lifetime of state e, whereas that of the α-β resonance is only about $0.5\,\mathrm{mT}$. In other words, superposition of the α-β resonance on the α-e resonance, i.e., the α-β-e three-level resonance interaction, makes it possible for atoms in α states to pass through spin filter without quenching. The three-level resonance is so sharp that it can be ob-

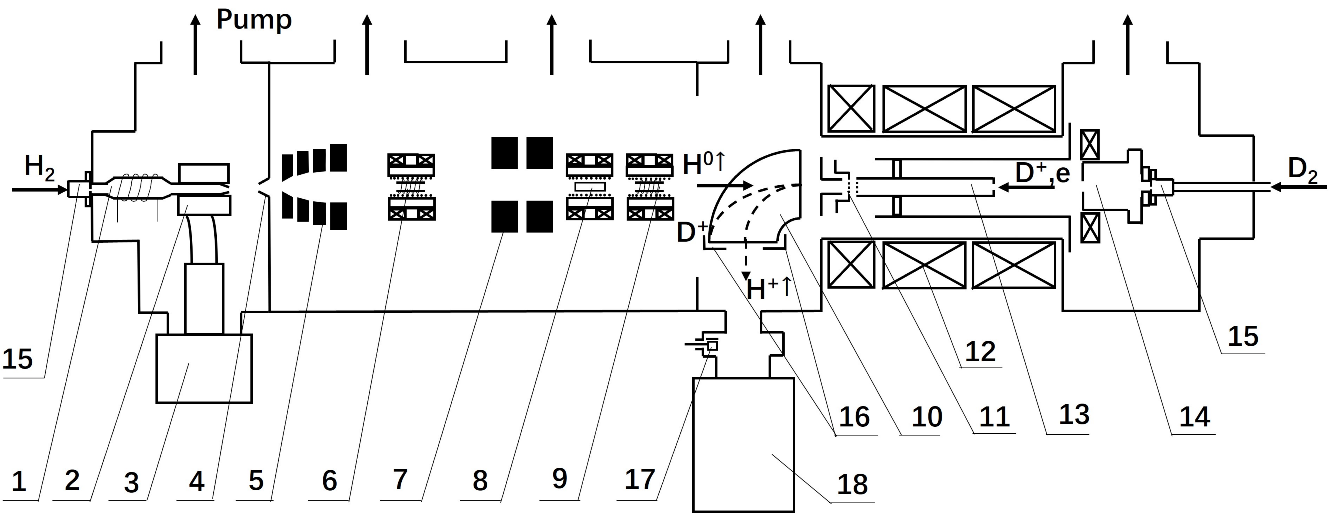

Fig. 1. Layout of the SPIS. (1) Dissociator, (2) cold copper clip, (3) refrigerator, (4) skimmer, (5 and 7) permanent sextupole magnet, (6) medium field RF transition unit, (8) strong field RF transition unit, (9) weak field RF transition unit, (10) bending magnet, (11) beam extraction system, (12) solenoid, (13) storage cell, (14) arc plasma source, (15) solenoid valve, (16) beam dump, (17) Faraday cup, (18) Lamb-shift polarimeter.

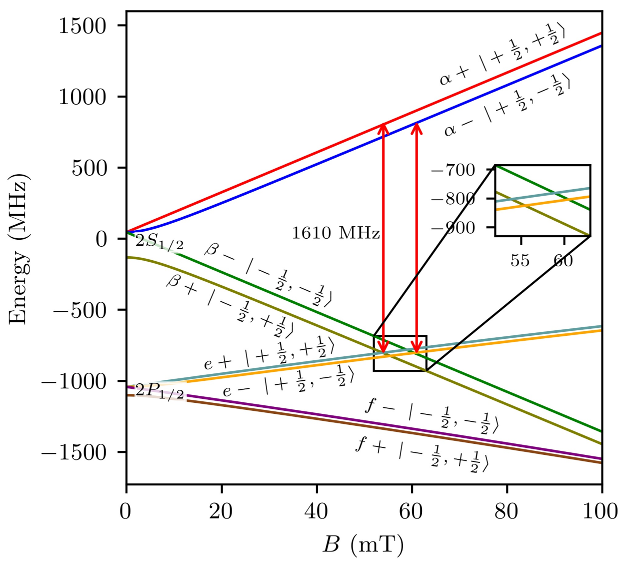

Fig. 2. The $2S_{1/2}$ and $2P_{1/2}$ levels of the hydrogen atom in an external magnetic field with nuclear hyperfine structure included.

served for each hyperfine state. As shown in the enlargement of Fig. 2, there are two resonances for hydrogen at 54.0 and 61.0 mT, corresponding to $m_I = \pm 1/2$, respectively. For deuterium, the resonances are at 56.4, 57.4, and 58.4 mT, corresponding to $m_I = +1, 0, -1$, respectively. With the B_s in the resonant values, all the metastable atoms are quenched within spin filter except ones in the resonant m_I state due to the three-level resonance. That is to say, spin filter can pick out the metastable atoms with a specific m_I by varying the magnetic field B_s.

The layout of the LSP at IMP is shown in Fig. 3. For making it feasible for the polarized H^+/D^+ beams extracted from the SPIS, an ion beam transport aiming at modifying the spin orientation and the energy of the beam is incorporated into the LSP, including an Einzel lens, a Wien filter and a deceleration lens. The polarized proton beam extracted from the SPIS is focused by the Einzel lens into the Wien filter, where spin orientations of the protons are rotated to the beam direction. In the deceleration lens the beam is decelerated from $25\,\mathrm{keV}$ to $2.5\,\mathrm{keV/u}$ to guarantee enough dwell time of the metastable atoms in the spin filter, which is the precondition for the spin filter to work properly [24]. After the deceleration lens, a portion of the protons are converted into metastable hydrogen atoms through charge exchange as they pass through a sodium oven, where a strong magnetic field is employed to prevent depolarization. Subsequently, a spin filter is utilized to quench all metastable atoms except ones with the selected m_I, depending on the magnetic field B_s of the spin filter. The residual metastable atoms are quenched later by a quenching lens, and the Lyman-α photons ($121\,\mathrm{nm}$), emitted by the transitions, are registered by a photomultiplier tube (PMT). As the metastable atoms with different m_I are selected in the spin filter, the number of photons counted by the PMT is proportional to the metastable atoms with the selected m_I, which in turn is proportional to the number of protons with the selected m_I in the primary ion beam. The beam polarization is determined directly. When the LSP is used to measure the deuteron beam polarization, the mixed H_2^+ ions also can be converted into metastable atoms at the sodium oven and the corresponding resonances will appear in the spin filter. But these resonances are clearly separated due to the distant resonance values of the magnetic field B_s. The polarization of the deuteron beam polarization can be measured without being affected. Because the beam produced by

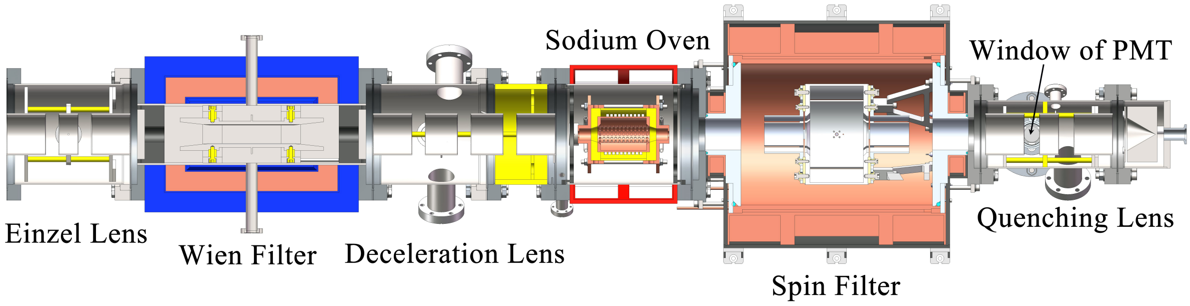

Fig. 3. Layout of the LSP at IMP.

the SPIS is pulsed, with an averaged intensity of $0.5\,\mu$A, in order to get adequate statistical precision as soon as possible, each component of the LSP is designed carefully to ensure high efficiency throughout every stage of the measurement process [25].

III. ION BEAM TRANSPORT

The ion beam transport line, shown in Fig. 4, is located between the ionizer and the sodium oven. As mentioned above, it modifies both the energy (velocity) and the spin orientation of the ion beam. Simultaneously, it is optimized to maximize the number of ions entering the acceptance of the downstream sodium oven and the spin filter, which enables higher statistic precision to be achieved in a shorter time.

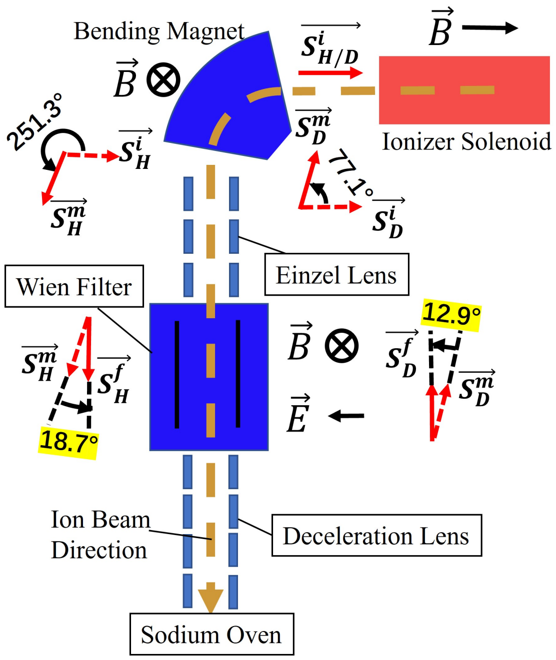

Fig. 4. Layout of the ion beam transport.

The red arrows in Fig. 4 represent the spin orientations of the polarized protons (deuterons). The original spin orientation $\vec{S}^i_{H/D}$ is determined by the magnetic field of the ionization region. After being bent by the dipole magnet, not only the beam direction is changed, but also the spin orientation. According to the Larmor procession equation,

$$\frac{d\vec{S}}{dt} = \vec{\mu} \times \vec{B} = g\frac{q}{2m}\vec{S} \times \vec{B}, \tag{4}$$

where $\vec{S}$ is the spin angular momentum, and $\vec{\mu}$, g, q, m the magnetic moment, g-factor ($g_p = 5.586$, $g_D = 1.714$), electric charge and ion mass of the particle, respectively. Therefore, $\vec{S}$ precesses around the opposite direction of the magnetic field with an angular frequency,

$$\omega_L = \frac{g}{2}\frac{q}{m}B_\perp, \tag{5}$$

where $B_\perp$ is the component of the magnetic field perpendicular to $\vec{S}$. Supposing that the effective length of the magnetic field is L and the particle's speed is v, the precession angle of $\vec{S}$ can be written as,

$$\phi = \omega_L \frac{L}{v} = \frac{g}{2}\frac{q}{mv}B_\perp L = \frac{g}{2}\frac{B_\perp L}{[B\rho]}, \tag{6}$$

where the relativity is ignored and $[B\rho]$ represents the particle magnetic rigidity. From Eq. (6) it is easy to obtain that if the dipole magnetic field deflects the ion beam by an angle of θ, the spin orientation will precess around the opposite direction of the dipole magnetic field by an angle of $g\theta/2$. As depicted in Fig. 4, after being bent by the dipole magnet, the spin orientation is rotated form $\vec{S}^i_{H/D}$ to $\vec{S}^m_{H/D}$. Based on the same principle, the Wien filter is used to rotate the spin of proton (deuteron) by a well-defined angle, from $\vec{S}^m_{H/D}$ to $\vec{S}^f_{H/D}$, to make it parallel (antiparallel) to the beam direction.

Space charge effect during the low energy ($25\,$keV) and high-current ion beam transport is inevitable [26]. Based on the quasi-resonant charge exchange ionization scheme, it is estimated that the extraction of a $1\,$mA polarized proton beam is accompanied by an unpolarized deuteron beam of about

50 mA [27]. Although the unpolarized deuterons can be separated out in the bending magnet, and almost all of the space charge effect in the bending magnet can be compensated by the electrons produced through collisions between ions and the residual gas molecules or beam loss at the vacuum chamber wall [28, 29]. In the subsequent electrostatic elements, there is almost no compensation for the space charge, as the neutralization electrons are rapidly repelled by the electric fields. For polarized deuteron beam the space charge effect is more serious, because they are always accompanied by unseparated H_2^+ ions.

To determine the optimal configuration of the ion beam transport line, a beam transport simulation was conducted. In the simulation, the beam was considered to be a direct current (DC) rather than a pulse. Fig. 5 shows the calculated evolution of the double rms envelop of deuteron beam of 6 mA (equivalent to D^+ and accompanied H_2^+ in intensity of 1 mA and 5 mA, respectively) and of 25 keV from the exit of the ion beam extraction system to the quenching gap faced by the PMT window. At the exit of the ion beam extraction system, the beam is cylindrically symmetric in KV distributions in vertical and horizontal directions and the initial Twiss parameters are set as follows:

$$\begin{aligned}\alpha_{x,y} = 0, \beta_{x,y} = 0.169\,\pi\text{mm mrad}^{-1},\\ \epsilon_{norm,rms,x,y} = 0.375\,\pi\text{mm mrad},\end{aligned}$$

adopting the result from previous experiments with a similar devices [27]. After the exit of the ion beam extraction system, there is a drift section of 100 mm before the dipole magnet. The dipole magnet bends the beam by 90° with a radius of 100 mm and provides focus force in both vertical and horizontal directions with a pair of inclined pole faces and a field decline indicator of 0.5 [30]. Subsequently, the beam drifts 425 mm reaching the entrance of the Einzel lens. The ion beam transport in this section is calculated by TraceWin code [31]. The three-dimensional magnetic field of the dipole magnet calculated by OPERA [32] is imported and the space charge effect is ignored. After the dipole magnet, the deuteron beam passes through the Einzel lens, the Wien filter, the deceleration lens and arrives at the sodium oven. At the middle plane of the sodium oven, the deuterons are assumed to be converted to metastable atoms. Following, the atoms drift through the spin filter and reach the quenching chamber. Simulation for the beam transport in this section was finished by IBSimu code [33]. Space charge effects are accounted for through multiple iterations. Particle trajectories are initially calculated without considering space charge. Subsequently, the corresponding space charge is incorporated based on the previously calculated trajectories, and this process is repeated until the solution converged to the required precision. The ion beam transport through each element is simulated sequentially, with the beam phase space distribution from the end of the last element being used as the initial condition for the next element. The transmission efficiency of the ion beam transport is defined as the ratio of the number of the particles arriving at the quenching gap to the initial number of the particles at the exit of the beam extraction system. According to the simulation, the transmission efficiency of the deuteron beam can be optimized to 4 %. For the proton beam, the maximum transmission reaches 8 %.

IV. SODIUM OVEN

In the sodium oven, a portion of protons (deuterons) is converted to metastable atoms through charge-exchange. The sodium oven is shown schematically in Fig. 6. To avoid depolarization, the sodium oven is installed in a solenoid producing a magnetic field of up to 70 mT, which is stronger than the critical field of the metastable hydrogen (deuterium) atom ($B^{2S}_{c,H} = 6.3$ mT, $B^{2S}_{c,D} = 1.5$ mT) [17]. Metal sodium is loaded into a reservoir made of copper. As the reservoir is heated by a coil heater, sodium vapor emerges into a cell channel through openings on it. Two end plates with a central hole of 10 mm limit the sodium vapor flowing into the neighboring elements. Between the end plate and the reservoir, thermal insulation material ($\mathrm{ZrO_2}$) is employed. Additionally, cooling water has been added to the two end plates. In this way, the temperature of the two end plates is always below the melting point of sodium (98 °C), which is conducive to reduce the sodium vapor diffusion into the neighboring elements.

For protons (deuterons) of 2.5 keV/u, the cross section of charge exchange for metastable atom production is about 1×10^{-15} cm^2 [34, 35]. The metastable atom yield depends on the thickness of the sodium target Π. According to the result of the previous experiments, the optimal target thickness Π should be 2×10^{14} cm^{-2}, and the maximum yield is about 0.1 [36, 37]. With a thinner target, it is more likely that the protons will pass through the target without colliding with the sodium atoms. However, with a thicker target, multiple collisions may occur before the protons exit, leading to the collisionally deexcitation of the metastable atoms.

The target thickness Π depends on the reservoir temperature. To determine a suitable reservoir temperature for achieving the optimal target thickness Π, the evaporation of sodium has been simulated using the Molecular Flow Module of COMSOL [38–40]. In the simulation, the bottom of the reservoir is set as an evaporation surface. The evaporation rate, i.e., the number of sodium atoms evaporated from the surface per unit area per unit time, is determined by the surface temperature as

$$Q = \alpha\sqrt{\frac{N_A^2}{2\pi MRT}}P_s(T), \tag{7}$$

where N_A is the Avogadro's number, $M = 23$ g/mol is the Molar mass of sodium, $R = 8.314$ J K^{-1} mol^{-1} is the gas constant, T [K] is the temperature of the evaporation face, α is the evaporation coefficient, and the $P_s(T)$ is the saturated vapor pressure of the sodium as a function of the temperature T [K]. The dependence of the P_s on the temperature is given by [41],

$$\lg P_s\,[\text{mmHg}] = -\frac{5567}{T\,[\text{K}]} - 0.5\lg T\,[\text{K}] + 9.235. \tag{8}$$

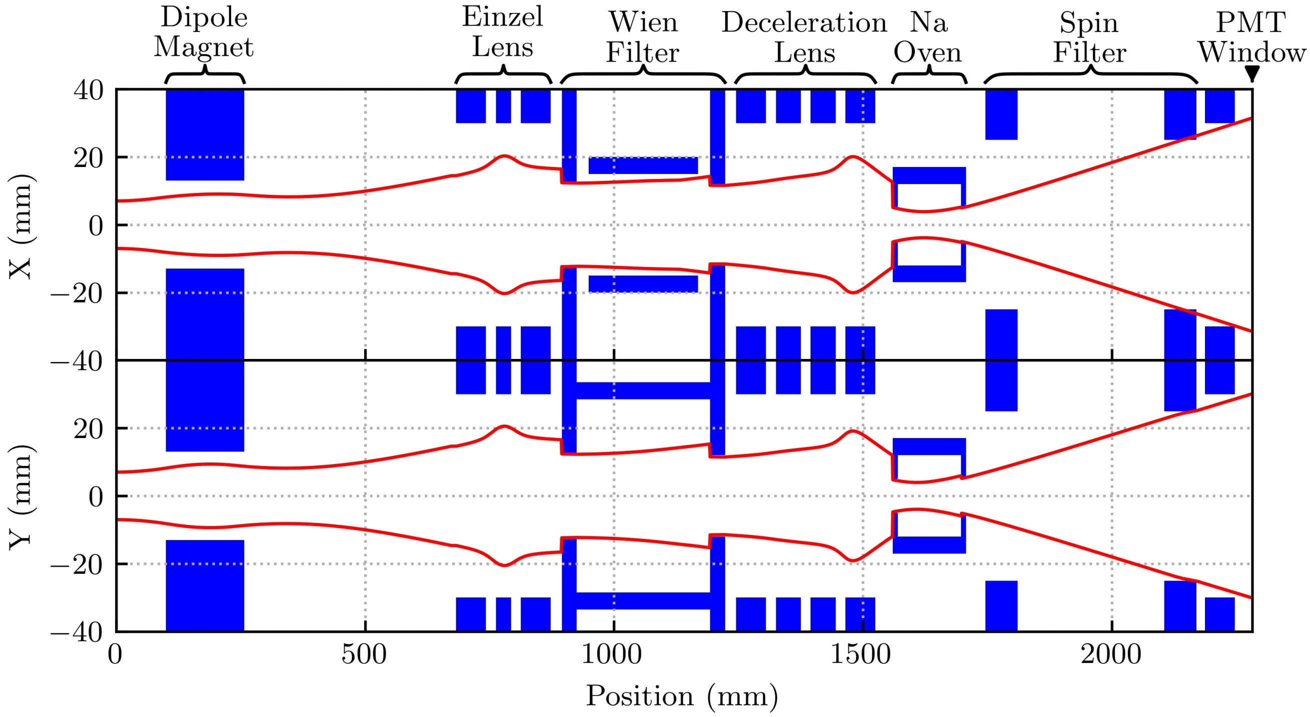

Fig. 5. The simulated double rms envelop of the deuteron beam of 6 mA and of 25 keV from the exit of the ion beam extraction system to the quenching gap faced by the PMT window. After being bent by the dipole magnet, the beam is focused by the Einzel lens, of which the middle electrode is on a potential of 15 kV. Then, at the Wien filter the beam spin orientation is rotated by an angle of $12.9°$ by its magnetic field. And the potential of the two plate electrodes of the Wien filter are $\pm$ 780 V, respectively. Following, in the deceleration lens the beam is decelerated from 25 keV to 5 keV. The potentials of the four cylinder electrodes are 0, 2, 1 and 20 kV, respectively. It is noticeable that all of the downstream elements behind the deceleration lens are floated at a potential of 20 kV. Subsequently, the deuterons are converted to metastable atoms at the sodium oven and drift to the quenching gap.

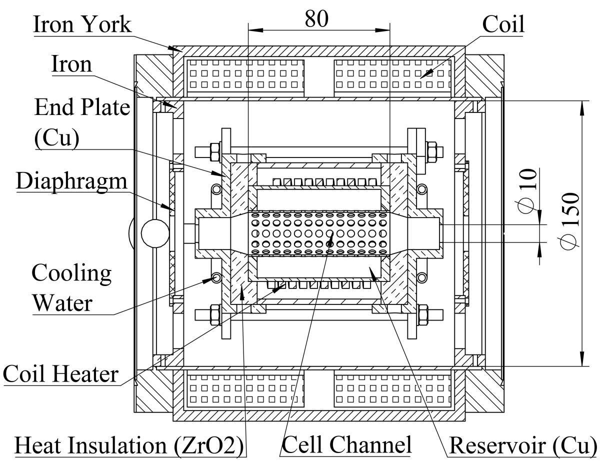

Fig. 6. Cross-sectional view of the sodium oven.

It is assumed that the sodium atoms are backscattered when they collide with the interior walls of the reservoir, while they will be absorbed when they collide with the other faces of the oven due to the low temperature of these faces. Fig. 7 (a) shows the simulated number density distribution of the sodium atoms along the axis of the oven for different reservoir temperatures. Outside the cell channel (-40 to 40 mm) the number density of sodium atoms decreases rapidly. The integration of the atom number density along the axis, i.e., the atoms thickness, is shown in Fig. 7 (b) as a function of the reservoir temperature. At 525 K, the sodium atoms thickness is about $2 \times 10^{14}\ \mathrm{cm}^{-2}$, a suitable value for production of the metastable atoms, and the average pressure of the reservoir is about 0.2 Pa. The actual operation temperature of the reservoir should be higher than 525 K, because the evaporation coefficient is set to the ideal value 1 in the simulation.

A steady-state thermal analysis of the sodium oven has been done with ANSYS [42]. The thermal conductivity of copper and ZrO_2 are set to 400 and 2 $\mathrm{W\,m^{-1}\,K^{-1}}$, respectively. The loop of cooling water on the end plate is designed carefully. At the inlet, the water speed and temperature are specified to $1.5\,\mathrm{m/s}$ and $20\,°\mathrm{C}$, respectively. At the outlet, the water pressure is set to 0 Pa. When the coil heater power is 300 W, the simulated steady-state temperature distribution is shown in Fig. 8. With a temperature of the reservoir of $250\,°\mathrm{C}$, the periphery of the sodium oven keeps a significantly lower temperature. According to further simulations, even with more heater power and reservoir temperature, such as $450\,°\mathrm{C}$, the periphery of the sodium oven is less than

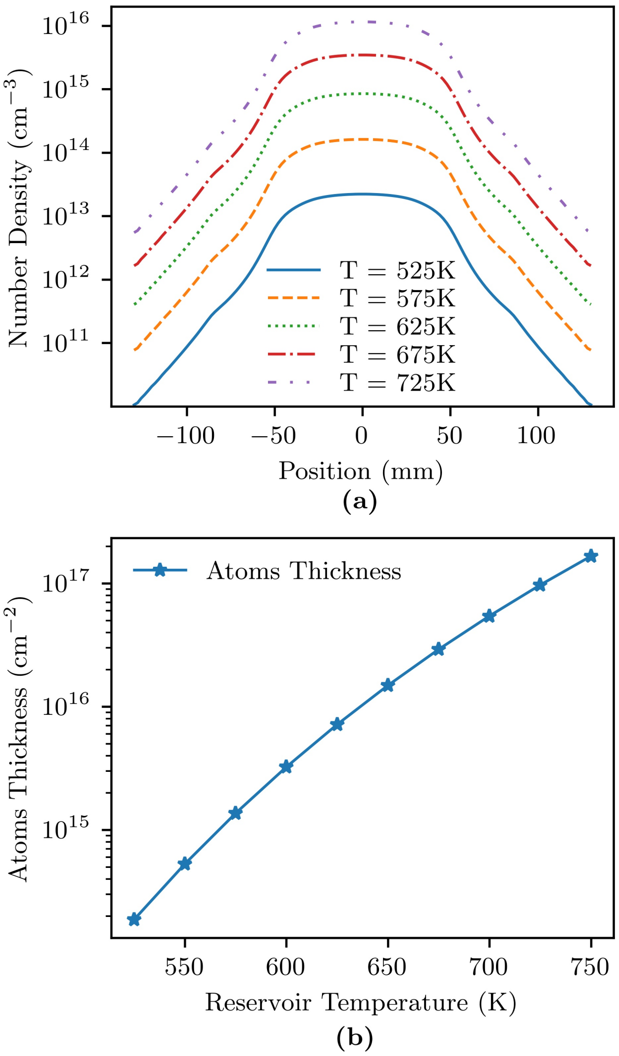

Fig. 7. The simulated number density distribution of the sodium atoms along the axis of the oven **(a)** and the target thickness **(b)** for different reservoir temperatures.

50 °C.

V. SPIN FILTER

The spin filter is shown schematically in Fig. 9. Its consists of a solenoid magnet and a RF resonant cavity. Because spin filter is based on the three-level resonance interaction, inadequate homogeneity of the static magnetic field (B_s) provided by the solenoid magnet can cause unexpected quenching of the metastable atoms. A successful spin filter applied for the polarimeter requires an axial magnetic field uniform to ± 0.05 mT over the central region of the spin-filter cavity [43]. The solenoid magnet comprises of five windings (C1, B1, A, B2 and C2), wound around copper skeletons. The system of the windings has been optimized with OPERA [32]. As shown by the insert of Fig. 10, the fluctuation of the solenoid magnetic field is less than ± 0.02 mT at 60 mT over the central region of the spin filter cavity. To shield the interference with the magnetic field uniformity caused by external fields, especially the fringe field from the upstream sodium oven, all of the windings are enclosed by iron yokes. In addition, to avoid the frequency shift of the RF resonant cavity led by thermal expansion, an interlayer for water cooling is designed in the copper skeleton, which effectively prevents the heat transfer from the windings to the cavity. It should be noted that the magnetic field in the spin filter must be parallel to the field in the sodium oven. Otherwise, unwanted Sona transitions may take place in the zero-crossing region, which will distort the polarization measurement results [44].

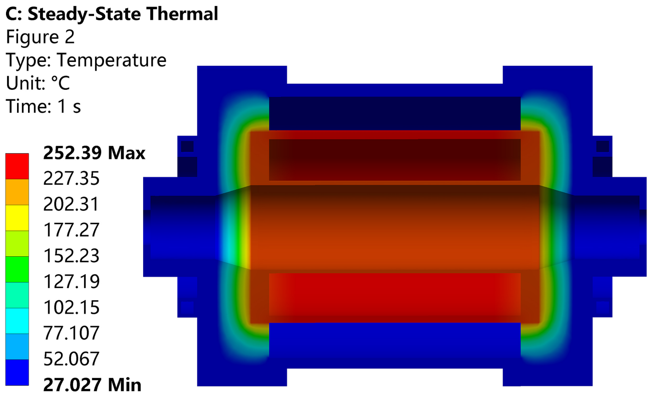

Fig. 8. The temperature distribution with a sectional view of the sodium oven from a steady state simulation with 300 W of heating power applied on the outside surface of the reservoir.

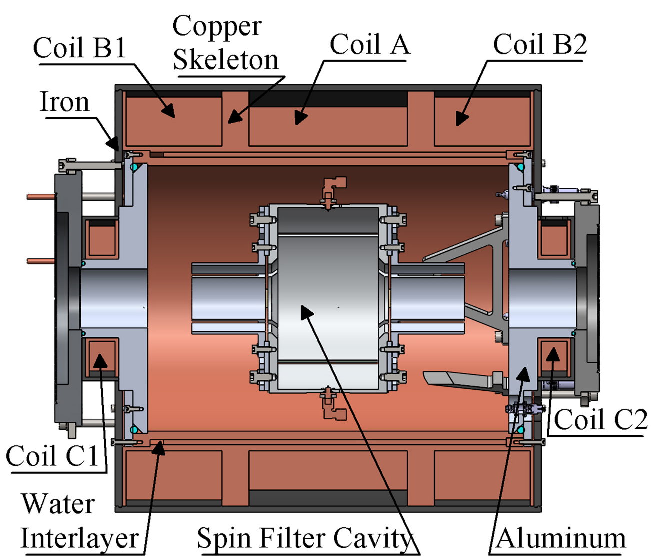

Fig. 9. Cross-sectional view of the spin filter.

The RF resonant cavity is a cylindrical cavity with a length of 82 mm and a radius of 75 mm. Each end of the cavity is fitted with an end pipe that has a smaller radius of 30 mm. The cavity is split into four sectors. One pair of opposing sec-

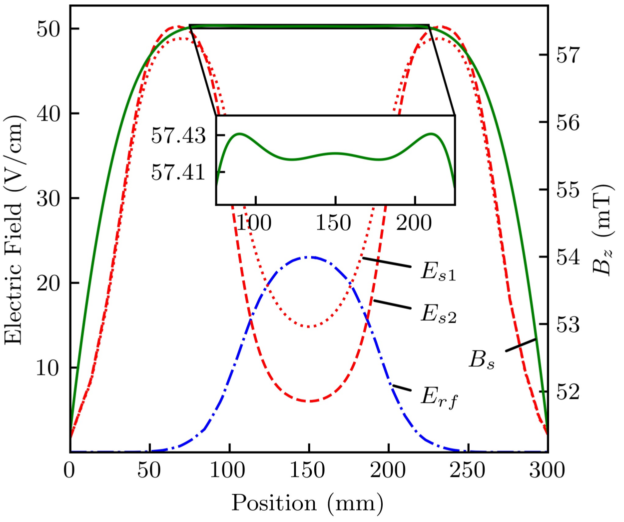

Fig. 10. The spin filter magnetic and electric fields distribution.

tors are grounded and serves the purpose of RF feeding and sampling. The other two sectors are applied with symmetric voltages, which are used to generate a transversal electric field inside the cavity. The slots between these sectors can be manipulated to fine-tune the cavity's resonance frequency to $1610\,\mathrm{MHz}$. Fig. 10 illustrates the simulated distribution of the longitudinal RF electric field with a dash-dotted (E_{rf}) line. Similarly, the two end pipes also are divided into four sectors. The sectors adjacent to the RF feeding and sampling sectors of the cavity are grounded, while the other two are floated and can be applied with symmetric voltages. This setup allows for the static electric field within the cavity and the end pipes to be altered independently. As shown by the dotted (E_{s1}) and dashed (E_{s2}) lines in Fig. 10, besides the transversal static electric field of 10–20 $\mathrm{V/cm}$ inside the cavity, an enhanced field of about $50\,\mathrm{V/cm}$ is established in the end pipes. This stronger field is designed to deflect protons (deuterons) that fail to capture an electron in the sodium oven. The deflection is essential, because the protons (deuterons) can reach the downstream quenching chamber. Their arrival induces a non-linear background signal in the PMT, which fluctuates with the magnetic field of the spin filter. This variability makes the signal processing challenging.

An effective spin filter should possess two key characteristics. First, it should exhibit a high transmission for metastable atoms in the resonant m_I states, facilitating the acquisition of high statistical precision in a shorter measurement time. Second, a good spin filter must demonstrate a high selectivity for metastable atoms with different m_I values, which is a fundamental requirement for accurate beam polarization measurement. Both, the transmission and the selectivity, are depending on various influencing factors, including the velocity of the metastable atoms, uniformity of the axial static magnetic field, and distributions of the static electric fields and the RF fields. While there are established general principles derived from prior calculations and experiments, an effective spin filter design entails a quantitative and comprehensive evaluation of the transmission and the selectivity under various spin filter design parameters.

The calculation can be conducted by employing a time-dependent quantum mechanical approach to analyze the atomic four-level system, α, β, e and f levels, as was done in the refs. [45, 46]. The spin filter operates in a magnetic field (50–60 mT) much stronger than the critical magnetic field B_c of hydrogen (deuterium) atom in 2S and 2P states. Therefore, the quantum number m_I is conserved and each group of the four atomic levels associated with the same m_I can be individually considered. The perturbed Schrödinger equation may be written as,

$$\left(\hat{H}_0 + \hat{H}'\right)\psi = \imath\hbar\frac{\partial\psi}{\partial t}, \tag{9}$$

where H_0 is a Hamiltonian including the influence of an ideal uniform static magnetic field, whose eigenfunctions satisfy the equation $H_0 u_0 = E_n u_n$, and H' symbolize perturbations of the RF fields, the static electric field and the fluctuated static magnetic field. Expanding the atomic wave function ψ with u_n,

$$\psi = \sum_n a_n(t) u_n e^{-\imath E_n t/\hbar}, \tag{10}$$

the coefficients $a_k(t)$ satisfy the differential equations,

$$\imath\hbar\dot{a}_k = \sum_n H'_{kn} a_n e^{\imath\omega_{kn} t}, \tag{11}$$

where

$$\omega_{kn} = \left(E_k - E_n\right)/\hbar,$$
$$H'_{kn} = \int u_k^* \hat{H}' u_n \mathrm{d}t.$$

The perturbation matrix elements H'_{kn} can be calculated and are given in ref. [46]. Damping terms accounting for the spontaneous decay of the e and f states also can be included in Eq. 11. A Python code has been written to calculate the time-evolution of the individual α, β, e and f state amplitudes, denoted as a, b, c and d by numerical integration of the Eq. 11.

As a metastable α-state deuterium atom with $m_I = 0$ going through the spin filter with an energy of $2.5\,\mathrm{keV/u}$, time-evolutions of $|a|^2$ and $|a|^2 + |b|^2$ for three different fields configurations are shown in the left plot of Fig. 11. Case ① has a uniform electrostatic field of $15\,\mathrm{V/cm}$, the realistic RF electric field and static magnetic field as shown respectively by the dash-dotted (E_{rf}) and solid (B_s) curves in Fig. 10. In case ② and ③, replace the uniform electrostatic field with the real one as shown by the dotted (E_{s1}) and dashed (E_{s2}) curves in Fig. 10, respectively. The central values of the E_{s1} and E_{s2} are 15 and 6 V/cm, respectively. Comparing the time-evolution curves, due to the deflection electric field at the entrance and exit of the spin filter, the decay of the metastable atom of case ② and ③ are more rapid than case ①. The adiabatic variation of $|b|^2$ with E_{rf}, as described in ref. [46], is clearly evident in the time-evolution curves. From the entrance to the exit of the spin filter, as E_{rf} increases gradually

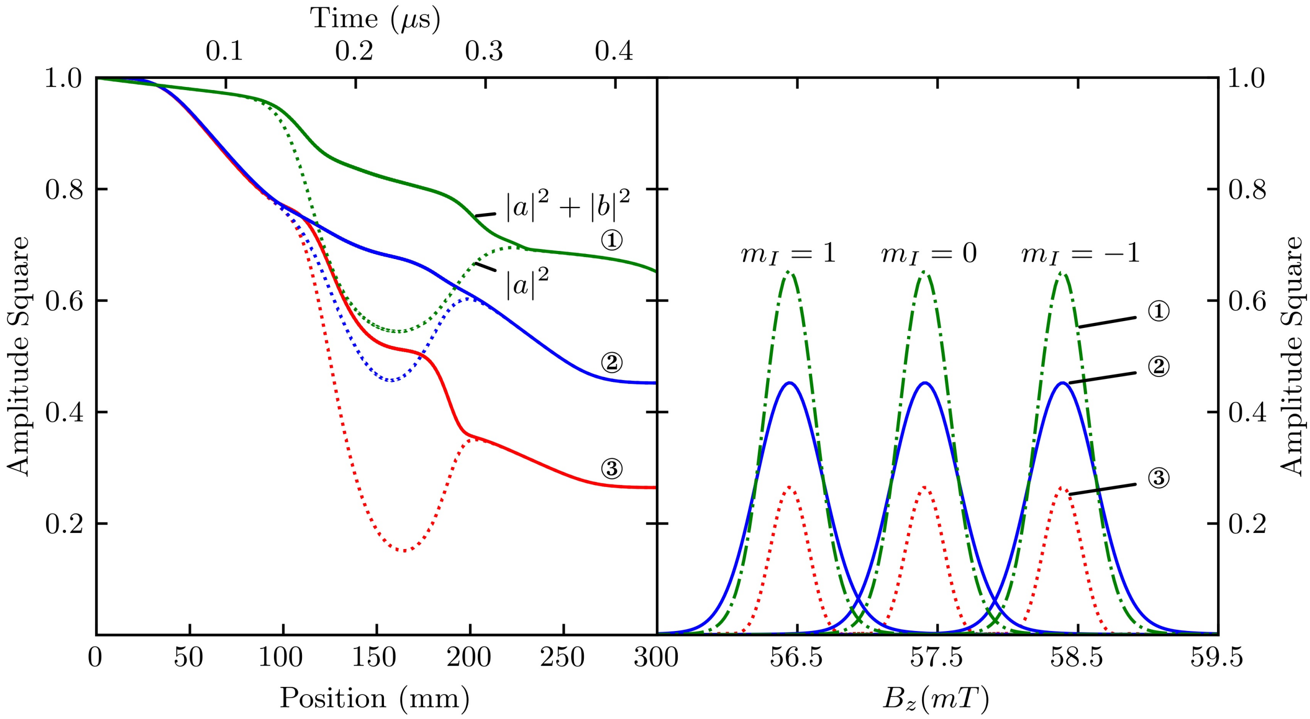

Fig. 11. Left plot shows the time-evolution of $|a|^2$ and $|a|^2 + |b|^2$, when a α-state deuterium atom with $m_I = 0$ going through the spin filter with a kinetic energy of $2.5\,\mathrm{keV/u}$, for three different fields configurations. Right plot shows the variations of the transmission for metastable deuterium atom with different m_I in these three cases.

the deuterium atom will be a coherent mixture of α and β states, and then as E_{rf} slowly decreases to zero the α and β mixture is transformed back into a pure α state. There is a sever adiabatic loss for case ③. With the central value of E_s increasing from 6 to 15 $\mathrm{V\,cm^{-1}}$, the adiabatic loss gradually diminishes, leading to an increase in the transmission. The calculated transmission of the metastable atom, represented as $|a|^2 + |b|^2$ at the exit of the spin filter, is a function of the B_s value. The value of B_s is swept from 55.5 to 59.5 mT, while maintaining its distribution as shown in Fig. 10. The variations of the transmission for metastable deuterium atom with different m_I in these three cases are illustrated in the right plot of Fig. 11, which also indicates the measurement spectra. Based on the calculated spectra, an increase in the central value of E_s leads to not only a higher transmission but also a spectrum with a larger width and a worse selectivity. Although the transmission in case ② is higher, it is unsuitable for separation of metastable deuterium atoms with different m_I due to the presence of overlapping between their resonant peaks. Case ②, however, is more favorable to be used for separation of metastable hydrogen atoms, because their two resonant peaks are more distant.

VI. DETECTION FOR METASTABLE ATOMS

As shown in Fig. 3, at the end the survival metastable atoms are quenched by the electric field of a quenching lens, and the emitted Lyman-α photons ($121\,\mathrm{nm}$) are registered by a PMT which is only sensitive to photons with wavelength of 110 to 200 nm. The lifetime of metastable hydrogen (deuterium) atom with a moderate electric field can be approximated as,

$$\tau = \left(\frac{19}{E}\right)^2 \times 10^{-6}\ \mathrm{s}, \tag{12}$$

where E is the magnitude of the electric field in $\mathrm{V/cm}$ [23]. The kinetic energy of the atomic beam is $2.5\,\mathrm{keV/u}$ (7×10^7 cm/s). In order to achieve a high detection efficiency for the metastable atoms at this energy, the first gap width and the electric field of the quenching lens are set to be $2\,\mathrm{cm}$ and $200\,\mathrm{V/cm}$, respectively. Under these conditions, the lifetime of the metastable atoms ($9\,\mathrm{ns}$) is much shorter than the drift time in the gap ($30\,\mathrm{ns}$), which ensures that all metastable atoms are quenched in the first gap. The window of the PMT is located $8\,\mathrm{cm}$ away from the beam axis and its effective diameter is $23\,\mathrm{mm}$, which gives a geometric acceptance of $0.5\,\%$. The quantum efficiency of the photocathode (made of CsI) is considered to be $10\,\%$. Overall, the detection efficiency for metastable atoms is about $0.05\,\%$.

VII. RESULTS AND DISCUSSION

Based on the quantitative analyses for all of the critical processes of the LSP, the number of the Lyman-α photons de-

tected at the quenching chamber can be calculated. A beam of protons (deuterons) with intensity of $1\,\mathrm{mA}$, 6×10^{15} ions per second, gets into the ion beam transport line, because of severe space charge effect, only $8\,\%$ ($4\,\%$) of the protons (deuterons) can be qualified to go through the downstream elements. At the sodium oven, $10\,\%$ of the protons (deuterons) are converted to metastable atoms. Half of the metastable atoms stay in α states (the other half stay in β states), as there is no polarization at the sodium target. In addition, the fractions of the α states atoms with $m_I=\pm1/2$ ($m_I=\pm1,0$) are $1/2$ ($1/3$) under the assumption that the proton (deuteron) beam is unpolarized. After traversing the spin filter, $45\,\%$ ($25\,\%$) of the α state hydrogen (deuterium) atoms with the selected m_I retain in metastable state. Considering the detection efficiency of $0.05\,\%$ for the metastable atoms at the quenching chamber, it is expected that the peak count rate of the PMT will be around 3×10^9 (5×10^8) photons per second. For each beam pulse lasting $100\,\mu\mathrm{s}$, the number of the detected photons is 3×10^5 (5×10^4) per pulse. Consequently, a statistical error of about $0.4\,\%$ will be obtained. To achieve a spectrum as depicted in the right plot of Fig. 11, it is necessary to ramp the magnetic field of the spin filter from 50 to 65 mT in increments of $0.3\,\mathrm{mT}$. The time allocated for each step should be $200\,\mathrm{ms}$, ensuring that at least one beam pulse occurs during each step. This approach allows the entire spectrum to be recorded within a total duration of $10\,\mathrm{s}$.

The background is considered to be dominated by collisions between the ground-state atoms produced by charge exchange in the sodium oven and the residual gas [20]. The flux of the ground-state atoms obtained from the sodium oven is $N\approx10^{14}$ atoms per second, which is three times that of the metastable atoms [37]. If the pressure in the quenching chamber is $p=1\times10^{-6}$ mbar, times of the collisions in front of the PMT window can be calculated as $n=N\cdot\pi d^2\cdot L\cdot p/kT\approx2\times10^9$ collisions per second, where $d=1\times10^{-10}$ m is the atom diameter, $L=2\,\mathrm{cm}$ is the length faced by the PMT window, $k=1.38\times10^{-23}$ J/K is Boltzmann's constant, $T=300\,\mathrm{K}$ is the room temperature. With the estimation that $10\,\%$ of the collisions produce 110–200 nm photons and that $0.05\,\%$ of them are detected by the PMT, the background count rate is about 10^5 s^{-1} in the beam duration. The signal-to-background ratio is expected to be $10^3\sim10^4$.

Some corrections are necessary due to systematic factors, and the corrections depend on the properties of the components of the LSP. The corrections can be determined with the polarimeter itself. A systematic error of about $0.4\,\%$ in the correction factors is reasonable [20]. Therefore, it is feasible to measure the pulsed polarized proton (deuteron) beam using the designed LSP with a precision of $1\,\%$ in a few seconds.

VIII. SUMMARY

A Lamb-shift polarimeter tailored for the pulsed high-current polarized H^+/D^+ ion source is investigated systematically in this study. Beam transport in the ion beam transport line engineered to match the polarized beam extracted from the ionizer with the LSP has been simulated and optimized. The design of the sodium oven transforming protons (deuterons) to be metastable atoms has been completed, whose operation status has been mastered by evaporation simulation and thermal simulation. A spin filter has been designed, including a system of solenoidal windings with a homogeneity better than $0.05\,\%$ and a specific RF resonant cavity. Time-evolution of the wave function of the metastable hydrogen (deuterium) atoms in the spin filter has been calculated with numerical integral. A metastable atom detection unit also has been designed. Based on these calculations, it is expected that the proton (deuteron) beam polarization can be measured with a precision of $1\,\%$ within a few seconds with the designed LSP assembled directly downstream the polarized ion source. The LSP is being fabricated and will be integrated in a test bench with the SPIS in 2025. It will be an indispensable tool for tuning and optimizing the SPIS at IMP to produce proton (deuteron) beams with higher polarization. In fact, the LSP is capable of measuring the polarization of $H^\pm/D^\pm$ [25], even for H_2^+/D_2^+ ion beams [47]. Coupled with an ionizer, the LSP can also be employed to measure the polarization of H/D gas targets.

[1] X. Cao, L. Chang, N.B. Chang, *et al.*, Electron ion collider in China. Nuclear Techniques **43**: 020001 (2020). doi: 10.11889/j.02533219.2020.hjs.43.020001

[2] D. P. Anderle, V. Bertone, X. Cao, *et al.*, Electron-ion collider in China. Front. Phys. **16**: 64701 (2021). doi: 10.1007/s11467-021-1062-0

[3] J.C. Yang, J.W. Xia, G.Q. Xiao, *et al.*, High intensity heavy ion accelerator facility (HIAF) in China. Nucl. Instrum. Meth. B **317**: 263-265 (2013). doi: 10.1016/j.nimb.2013.08.046

[4] X.H. Zhou, J.C. Yang, the HIAF Project team, Status of the high-intensity heavy-ion accelerator facility in China. AAPPS Bull. **32**: 35 (2022). doi: 10.1007/s43673-022-00064-1

[5] R. Wang, X.R. Chen, The current status of electron ion collider in China. Few-body Syst. **63**: 48 (2022). doi: 10.1007/s00601-022-01751-3

[6] C.H. Zeng, T.B. Liu, P. Sun, *et al.*, Toward three-dimensional nucleon structures at the Electron-Ion Collider in China: A study of the Sivers function. Phys. Rev. D **106**: 094039 (2022). doi: 10.1103/PhysRevD.106.094039

[7] Z. Ji, X.Y. Zhao, A.Q. GUo, *et al.*, Lambda polarization at Electron-ion collider in China. Nucl. Sci. Tech. **34**: 155 (2023). doi: 10.1007/s41365-023-01317-w

[8] M.X. Li, J.C. Yang, W.S. Wu, *et al.*, Maintaining polarization with a constant field solenoid Siberian snake in the EicC-BRing. Nucl. Instrum. Meth. A **1031**: 166405 (2022). doi: 10.1016/j.nima.2022.166405

[9] A.S. Belov, Polarized ion sources: status and perspective. Phys. Part. Nuclei **44**: 873 (2013). doi: 10.1134/S1063779613060038

[10] A. Zelenski, Review of polarized ion source. Int. J. Mod. Phys.: Conference Series **40**: 1660100 (2016). doi:

10.1142/S2010194516601009

[11] A.S. Belov, Production of polarized ions with nearly resonant charge-exchange collisions in plasma. AIP Conf. Proc. **980**: 209 (2008). doi: 10.1063/1.2888089

[12] R. Gebel, O. Felden, R. Maier, Polarized H^- and D^- beams at COSY/Jülich. AIP Conf. Proc. **980**: 231 (2008). doi: 10.1063/1.2888091

[13] V.V. Fimushkin, *et al.*, in SPIN2018: The source of polarized ions (SPI) and low energy polarimeter for the NUCLOTRON facility, ed. by P. Lenisa, *et al.*. 23rd International Spin Physics Symposium, Ferrara, Italy, September, 2018. (Sissa Medialab, Trieste, Italy, 2019) doi: 10.22323/1.346.0114

[14] V.P. Derenchuk, A.S. Belov, Polarized D^- operation and development of the IUCF ion source CIPIOS. AIP Conf. Proc. **675**: 887 (2003). doi: 10.1016/j.nima.2023.168494

[15] A. Zelenski, G. Atoian, E. Beebe, *et al.*, Optically pumped polarized $^3He^{++}$ ion source development for RHIC/EIC. Nucl. Instrum. Meth. A **1055**: 168494 (2023). doi: 10.1016/j.nima.2023.168494

[16] A.S. Belov, S.K. Esin, L.P. Netchaeva, *et al.*, Polarized ions from a storage cell. AIP Conf. Proc. **421**: 362 (1998). doi: 10.1063/1.55006

[17] W. Haeberli, Source of polarized ions. Annu. Rev. Nucl. Sci. **17**: 376 (1967). doi: 10.1146/annurev.ns.17.120167.002105

[18] R. Bieber, A. M. van den Berg, K. Ermisch, *et al.*, Performance of the KVI in-beam polarimeter. Nucl. Instrum. Meth. A **457**: 12-21 (2001). doi: 10.1016/S0168-9002(00)00741-5

[19] S.K. Lemieux, T.B. Clegg, H.J. Karwowski, *et al.*, A spin-filter polarimeter for low energy hydrogen and deuterium ion beams. Nucl. Instrum. Meth. A **333**: 434-442 (1993). doi: 10.1016/0168-9002(93)91188-S

[20] R. Engels, R. Emmerich, J. Ley, *et al.*, Precision Lamb-shift polarimeter for polarized atomic and ion beams. Rev. Sci. Instrum. **74**: 4607-4615 (2003). doi: 10.1063/1.1619550

[21] G.P. Lawrence, G.G. Ohlsen, J.L. McKibben, Source of polarized negative hydrogen and deuterium Ions. Phys. Lett. B **28**: 594-596 (1969). doi: 10.1016/0370-2693(69)90195-6

[22] W.E. Lamb, R.C. Retherford, Fine structure of the hydrogen Atom. Part II. Phys. Rev. **81**: 222-232 (1951). doi: 10.1103/PhysRev.81.222

[23] W.E. Lamb, R.C. Retherford, Fine structure of the hydrogen atom. Part I. Phys. Rev. **79**: 549-572 (1950). doi: 10.1103/PhysRev.79.549

[24] H.R. Kremers, J.P.M. Beijers, N. Kalantar-Nayestanaki, Design and performance of the Lamb-shift polarimeter. Nucl. Instrum. Meth. A **536**: 329-333 (2005). doi: 10.1016/j.nima.2004.08.093

[25] Simon J. Pütz, *et al.*, in PSTP2022: Polarization measurement of a pulsed H^-/D^- ion Beam with a Lamb-shift Polarimeter, ed. by Alexander Nass, *et al.*. 19th Workshop on Polarized Sources, Targets and Polarimetry, Mainz, Germany, August, 2022. (Sissa Medialab, Trieste, Italy, 2023) doi: 10.22323/1.433.0029

[26] S.X. Peng, *et al.*, in HB2016: Study on space charge compensation of low energy high intensity ion beam in Peking University, ed. by Mohammad Eshraqi,*et al.*. 57th ICFA Advanced Beam Dynamics Workshop on High-Intensity, High Brightness and High Power Hadron Beams, Malmö, Sweden, 2016. (JACoW, Geneva, Switzerland, 2016) doi:10.18429/JACoW-HB2016-WEPM6Y01

[27] A.S. Belov, S.K. Esin, S.A. Kubalov, *et al.*, Pulsed high-intensity source of polarized protons. Nucl. Instrum. Meth. A **255**: 442-459 (1987). doi: 10.1016/0168-9002(87)91211-3

[28] D. Winklehner, Ion beam extraction from electron cyclotron resonance ion source and the subsequent low energy beam transport. Michigan State University, (2013).

[29] Z. Shen, Studies on ion beam extraction from high-intensity highly charged ECR ion sources and the space charge effect, Institute of Modern Physics, Chinese Academy of Sciences, (2022).

[30] Y.G. Liu, Q. Wu, X. Zhang, *et al.*, Design of a 180° electromagnetic isotope separator with inhomogeneous magnetic field. Nucl. Instrum. Meth. A **1006**: 165428 (2021). doi: 10.1016/j.nima.2021.165428

[31] TraceWin, https://www.dacm-logiciels.fr/tracewin, 2024-10-20.

[32] OPERA, https://www.3ds.com/products/simulia/opera, 2024-10-20.

[33] T. Kalvas, O. Tarvainen, T. Ropponen, *et al.*, IBSIMU: A three-dimensional simulation software for charged particle optics. Rev. Sci. Instrum. **81**: 02B703 (2010). doi: 10.1063/1.3258608

[34] T. Nagata, Charge changing collisions of atomic beams in alkali-metal vapors. IV. Total cross sections for single-electron capture by H^+ ion and H(1S) atom. J. Phys. Soc. Jpn. **48**: 2068-2075 (1980). doi: 10.1143/JPSJ.48.2068

[35] C.H. Liu, Y.Z. Qu, L. Liu, *et al.*, Charge transfer and excitation in slow proton collisions with sodium. Phys. Rev. A **78**: 024703 (2008). doi: 10.1103/PhysRevA.78.024703

[36] P. Pradel, F. Roussel, A.S. Schlachter, *et al.*, Formation of H ($n = 2$) atoms by the nearly resonant process H^+ in Cs. multiple collision processes. Phys. Rev. A **10**: 797-812 (1974). doi: 10.1103/PhysRevA.10.797

[37] T. Nagata, Charge changing collisions of atomic beams in alkali-metal vapors. III. Formations of H(2S) atoms from H^+ ions. J. Phys. Soc. Jpn. **46**: 1622-1627 (1979). doi: 10.1143/JPSJ.46.1622

[38] COMSOL, https://cn.comsol.com/molecular-flow-module, 2024-10-20.

[39] X.X. Lian, D.W. Zhong, Modeling and simulation of lithium vacuum evaporation process using COMSOL Multiphysics. J. Therm. Sci. **33**: 86-100 (2024). 10.1007/s11630-023-1914-8

[40] Y.C. Guo, Z.L. Su, Z.G. Li, *et al.*, Numerical investigation on the startup performance of high-temperature heat pipes for heat pipe cooled reactor application. Nucl. Sci. Tech. **32**: 104 (2021). 10.1007/s41365-021-00947-2

[41] R.W. Ditchburn, J.C. Gilmour, The vapor pressures of monatomic vapors. Rev. Mod. Phys. **13**:310-327 (1941). doi: 10.1103/RevModPhys.13.310

[42] ANSYS, https://www.ansys.com/zh-cn/products/structures/ansys-mechanical#tab1-1, 2024-10-20.

[43] C.D. Roper, T.B. Clegg, A.J. Mendez, Electromagnetic field requirements for a Lamb-shift spin-filter polarimeter. AIP Conf. Proc. **343**: 132-136 (1995). doi: 10.1063/1.48843

[44] P.G. Sona, New method proposed to increase polarization in polarized ion sources of H^- and D^-. Energ. Nucl. **14**: 295-299 (1967).

[45] W.E. Lamb, R.C. Retherford, Fine structure of the hydrogen atom. Part III. Phys. Rev. **85**: 259-276 (1952). doi: 10.1103/PhysRev.85.259

[46] G.G. Ohlsen, J.L. Mckibben, Theory of a radio frequency spin filter for a metastable hydrogen, deuterium, or tritium atomic beam (No. LA-3725). Los Alamos National Lab.(LANL), Los Alamos, NM (United States). (1967). doi: 10.2172/4517131

[47] R. Engels, R. Gorski, K. Grigoryev, *et al.*, Measurement of the nuclear polarization of hydrogen and deuterium molecules using a Lamb-shift polarimeter. Rev. Sci. Instrum. **85**: 103505

(2014). doi: 10.1063/1.4897479